3-D Radar Imaging of E-Region Field-Aligned Plasma Irregularities by Using Multireceiver and Multifrequency Techniques

Jenn-Shyong Chen, *Member, IEEE*, Chien-Ya Wang, Yen-Hsyang Chu, Ching-Lun Su, and Hiroyuki Hashiguchi

***Abstract*— This paper reports the first use of a 3-D radar imaging for observing E-region field-aligned plasma irregularities (FAIs) in the midlatitude ionosphere. Five carrier frequencies equally spaced between 46.25 and 46.75 MHz were transmitted alternately with consecutive radar pulses, and 20 receivers were employed for receiving the radar echoes. The experiments were carried out using the middle and upper atmosphere radar (34.85°N, 136.10°E), with the radar beams steered to the geographic north and 6.6° north by east, at the zenith angles of 51.0° and 51.5°, respectively. The 2-D imaging with the echoes collected by the 19 of the 20 receivers revealed that in zonal dimension, the off-beam direction of arrival (DOA) of the echo region changed alternately between positive and negative values, which can be attributed to the highly localized FAIs drifting zonally through the radar beam. On the other hand, the off-beam DOA in meridional dimension was negative and positive, respectively, at higher and lower range locations, which were supposed to be due to the meridional drift component of FAIs. A combination of 5 frequencies and 19 receivers achieved a 3-D imaging of the FAI structures, illustrating small-scale FAI striations and bubblelike plasma structures in the radar volume. Moreover, declination of geomagnetic field line was examined from the imaged 3-D brightness distribution in the radar volume; the estimated declination of geomagnetic field line was in agreement with that computed from the International Geomagnetic Reference Field model in 2011. This paper has demonstrated some capabilities of radar imaging for ionospheric investigation.**

***Index Terms*— Direction of arrival (DOA) estimation, ionosphere, radar imaging, very high-frequency (VHF) radar.**

Manuscript received November 21, 2016; revised May 4, 2017, January 31, 2018, and March 7, 2018; accepted March 14, 2018. Date of publication August 23, 2018; date of current version September 25, 2018. This work was supported in part by the Ministry of Science and Technology of Taiwan under Grant MOST104-2111-M-039-001 and Grant MOST105-2111-M-039-002-MY2 and in part by the International Collaborative Research Program of the Middle and Upper Radar. *(Corresponding author: Jenn-Shyong Chen.)*

J.-S. Chen is with the Center for General Education, China Medical University, Taichung 40402, Taiwan (e-mail: james.chen@mail.cmu.edu.tw).

C.-Y. Wang is with the Department of Optoelectric Physics, Chinese Culture University, Taipei 11114, Taiwan (e-mail: cywang@faculty.pccu.edu.tw).

Y.-H. Chu and C.-L. Su are with the Graduate Institute of Space Science, National Central University, Taoyuan 32001, Taiwan (e-mail: yhchu@jupiter.ss.ncu.edu.tw).

H. Hashiguchi is with the Research Institute for Sustainable Humanosphere, Kyoto University, Kyoto 606-8501, Japan (e-mail: hasiguti@rish.kyoto-u.ac.jp).

Color versions of one or more of the figures in this paper are available online at http://ieeexplore.ieee.org.

Digital Object Identifier 10.1109/TGRS.2018.2818331

I. Introduction

BASED on the theoretical and simulating works made in [1], the first operational 3-D radar imaging using multiple receivers and multiple frequencies for the lower atmosphere was demonstrated in [2]. However, the follow-up survey with the same technique for the atmosphere was rare. In the literature, extended examinations of 3-D radar imaging were made in [3]–[5], using the same very high-frequency (VHF) radar facility employed in [2]: the middle and upper atmosphere radar (MUR; 34.85°N, 136.10°E; operated at 46.5 MHz) for the lower atmosphere. It is not surprised at a small quantity of study using the 3-D radar imaging at the VHF band, because adequate receivers and carrier frequencies are necessary for practical operation. The MUR is one of the few radars that can achieve the capability of 3-D radar imaging for the atmosphere. Another VHF radar that can fulfill multireceiver and multifrequency operations in the near future is the Middle Atmosphere Alomar Radar System in Norway [6]. In this paper, we extended the work made in [7] for the E-region field-aligned plasma irregularities (FAIs) and demonstrated a 3-D structure of FAIs in the radar volume for the first time.

The morphology of FAIs in the ionosphere is unique for the VHF-band atmospheric radar, as reported initially in [8]. Characteristics of FAIs, such as the positive and negative slopes of range versus time (termed "range rate") and quasi-periodic (QP) appearance, have brought researchers a great interest to pursue their occurring mechanisms. Dynamic motions, such as semidiurnal neutral-wind variation, atmospheric gravity wave, E_s layer instability, wind shear instability, and so on, were thus proposed [9]–[15].

Before this paper, several examinations of ionosphere with either multireceiver or multifrequency technique, termed, respectively, coherent radar imaging (CRI) [16] and range imaging (RIM) [17] (or frequency-domain radar interferometric imaging [18]), have been carried out. For example, Hysell *et al.* [19] used 4 and Saito *et al.* [20] used 19 receiving channels of the MUR for the 2-D radar imaging to determine the motion of QP echoes. With the three receivers of the Chung-Li VHF radar, Chu and Yang [21] and Wang *et al.* [22] have tried to examine the spatial structures of FAIs and sporadic E layer, and in a later study, Chu *et al.* [23] went deep into the plausible mechanisms of different types of

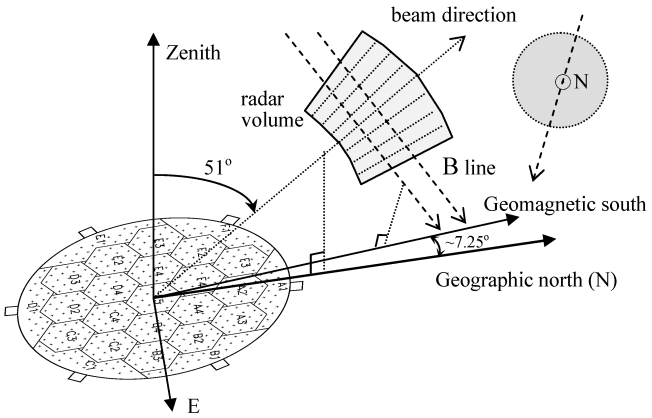

Fig. 1. Experimental setup of the MUR for observation of FAIs. The numbers of A1–F5 denote 25 antenna groups. The gray circle in the top-right corner is the cross section of radar beam, and also shown is the declination of geomagnetic field line (the B line in dashed) through the cross section of radar beam. In this paper, the circular full array was used for transmission and the radar beam was steered to the geographic north and 6.6° north by east, at 51° and 51.5° zenith angles, respectively.

plasma structures. Studies of the equatorial F-region over the Jicamarca Radio Observatory were also made with several receivers to observe the evolution of ionospheric irregularities [24]–[26]. More applications of multireceiver technique include the distribution of precipitation in the radar volume [27], measurement of aspect sensitivity [28], Sporadic *E* ionization layers and FAIs in the daytime subauroral ionospheric E-region [29], and so on. Using multifrequency RIM, on the other hand, Chen *et al.* [7] resolved finer striations in the FAI clusters and also identified the range sidelobe echoes due to pulse coding mechanism in the range-imaged brightness distribution. Based on these achievements, a 3-D radar imaging of the FAI structures in the radar volume can be implemented. It is expected that the finer FAI structures or plasma irregularities examined by 3-D radar imaging may offer studies on initial development in the instability process of plasma irregularities and other extended applications to the ionosphere in the future.

Section II describes the radar experimental setup. Section III shows the 1-D RIM and 2-D angular imaging of FAIs. The direction of arrival (DOA) of the major echo region was estimated from the 2-D angular brightness distribution, and the results could be associated with the drift of FAIs. The 3-D radar imaging is demonstrated in Section IV, and an application of estimating the declination of geomagnetic field line from the imaged 3-D brightness distribution in the radar volume is shown in Section V. Conclusions are stated in Section VI.

II. Experimental Setup

Fig. 1 shows the diagram of the radar experiment using the MUR for observing the FAIs. The radar array is composed of 475 crossed-Yagi antennas, each with a transceiver, and covers a circular area with a diameter of about 103 m. These antennas can be partitioned into 25 subarrays for 25 receiving channels, as indicated from A_1 to F_5 in Fig. 1. Each subarray consists of 19 antennas, and these subarrays can also be combined arbitrarily in software for receiving as well as for transmitting power (peak power 1 MW and on average 50 kW when using the full array). The multibeam technique is flexible: beam directions can be set with an angular step less than 1°, and the maximum number of beam directions is 256. The maximum number of frequencies is five for RIM, maximum span of frequencies is ±500 kHz with respect to the central frequency (46.5 MHz), and the frequency step unit is kHz. A pulse waveform is a modified rectangular for fitting in with the bandwidth of 3.6 MHz. Multireceiver and multifrequency modes can be set concurrently, but multibeam and multifrequency modes cannot execute simultaneously due to limitations of radar control and data processing. Pulse coding includes complementary and Barker codes, and the codes are user-defined. A more detailed description of the MUR upgraded since 2004 can be referred to [2].

For observations of FAIs, the radar beam was steered to the geographic north and 6.6° north by east at 51° and 51.5° zenith angles, respectively. The boresight of the oblique beam was perpendicular to the geomagnetic field line (B line hereafter) at an altitude of approximately 100 km, where FAIs occur frequently. Perpendicularity between the beam axis and the B line allows stronger echoes coming into the receiving antennas due to high aspect sensitivity of FAIs in the direction of the B line. With such a large zenith angle and a northward radar beam, two significant sidelobes in the radiation pattern appear at around 120° and 240° azimuth, and both at elevation angles less than 20° [30]. These sidelobes are blocked by the banks around the antenna array and thus have a little influence on FAI echoes. In addition to perpendicularity between the beam axis and the B line, the whole antenna array was operated for transmission to get stronger echoes, providing one-way half-power full beam widths of approximately 5.4° and 4.6° in zenithal and azimuthal directions, respectively. These beamwidths are slightly larger than those of a vertically transmitted beam (∼3.6°). Since FAI echoes have high aspect sensitivity along the B line, the echoes are usually confined within a small extent along the B line. On the other hand, a wider echoing region in the zonal dimension can be observed (shown later in Figs. 6 and 8); this has been applied to investigating the declination angle of B line in this paper. The declination of B line around the altitude of 100 km in the viewing region of the radar beam was about 7.25°, as estimated by the 2011 International Geomagnetic Reference Field (IGRF) model.

To fulfill 3-D radar imaging, the 19 subarrays, A2–A4, B2–B4, C2–C4, D2–D4, E2–E4, and F2–F5, were used for receiving the echoes, and the five frequencies, 46.25, 46.375, 46.5, 46.625, and 46.75 MHz, were transmitted with sequential radar pulses. Besides, the whole array was used as one of the 20 receiving channels for RIM. Interpulse period was 0.0015 s and coherent integration time was 2, giving a sampling time of 0.015 s under the operation of five frequencies. Radar pulse length was 4 μs, giving a range resolution of 600 m. Sampling step was 4 μs, sampling gate number was 128, and the sampling range interval was between 120 and 196.8 km, corresponding to the height interval approximately between 75.518 and 123.850 km for a radar beam directed to the

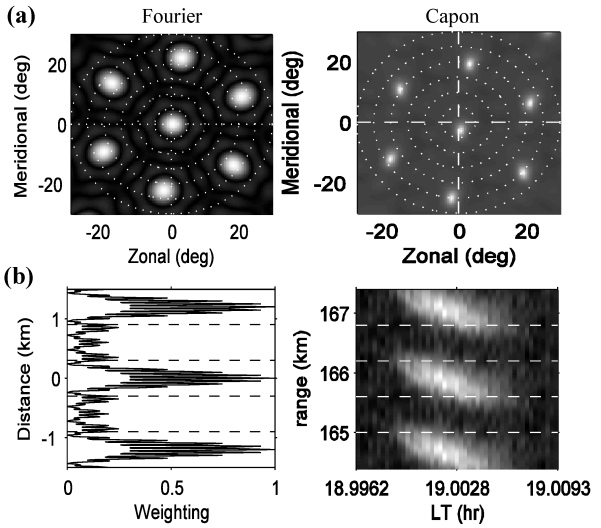

Fig. 2. Grating lobe patterns of (a) CRI and (b) RIM operations. The Fourier patterns are calculated from the theoretical weighting matrix, and the Capon patterns are retrieved with a true data set (self-normalized). Angle and range steps are 0.25° and 10 m, respectively, in the calculation.

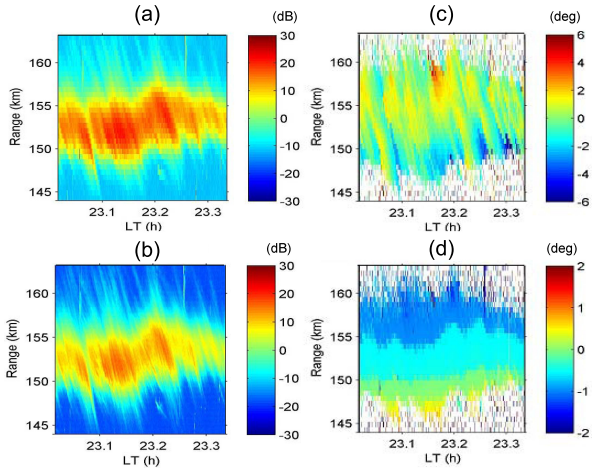

Fig. 3. (a) Range–time intensity plot of FAIs, (b) RIM, (c) zonal DOA, and (d) elevation DOA with respect to the beam center, observed on August 28, 2014.

geographic north and tilted to 51° zenith angle (ignore the curvature of the Earth's surface).

The radar data used in this paper were collected, respectively, on August 28 and 29, 2014 without pulse coding, on August 17, 2014 with 16-element binary complementary codes (1110110111100010 and 1110110100011101), and on August 1 and 2, 2016 without pulse coding. The radar beam was steered to the geographic north and 6.6° north by east, respectively, during the observations in 2014 and 2016. We have carefully dealt with the coded data according to the study made in [7]; the range sidelobe echoes due to coding mechanisms were excluded from analysis. Moreover, the grating lobe patterns of the imaging due to finite receiver separation and finite frequency step should be identified to restrict the imaging space. Fig. 2(a) and (b) displays the weighting patterns of CRI and RIM operations based on the array configuration and operating frequencies, respectively. Fig. 2 (left) was the theoretical patterns of the Fourier method, and the patterns in Fig. 2 (right) were obtained with a true data set and from the Capon method [16], [17]. The Capon method is an adaptive approach and its optimal weighting pattern depends on the distribution of the target; therefore, we can only inspect its grating lobe pattern from a practical retrieval. In Fig. 2(a), the zonal and meridional angles are relative to the beam axis direction. In Fig. 2(b), the ordinates of the left and right are, respectively, relative to the range gate center and the radar site along the beam axis direction. As shown, the Fourier patterns of CRI and RIM reveal several significant grating lobes at the separations of about 22.5° and 1.2 km, respectively. Analogously, the Capon patterns show the same features. In view of this, we have limited the imaging space within ±12° and ±600 m to avoid using the aliasing image.

III. 1-D AND 2-D RADAR IMAGING

RIM and CRI produce, respectively, 1-D range and 2-D angular brightness (power density) distributions in the radar volume. These imaged results, however, are still smoothened versions of the actual scales owing to many restrictions, such as finite numbers of receivers and transmitting frequencies, beamwidth, and so on. In spite of such a limitation, RIM and CRI indeed yield a better prospect to inspect the smaller structures in the radar volume of a pulsed radar.

Fig. 3 shows a segment of FAI echoes. The initial range–time intensity in Fig. 3(a) shows plentiful echoes. The RIM brightness in Fig. 3(b), obtained with the imaging step of 4 m, offers a sharper and smoother illustration of the striations. The 2-D angular brightness distribution for each range gate and each time is not displayed here. Instead, the zonal and meridional off-beam DOAs of the major echo regions are shown in Fig. 3(c) and (d), respectively, which were estimated from the angular brightness distribution. Here, in Fig. 3(d) and there in other illustrations, the meridional off-beam DOA is denoted as the elevation DOA, which is relative to the beam center; readers shall not confuse with the elevation angle relative to the horizontal. Since the FAIs are highly localized in the field-aligned dimension, the beam weighting effect was not corrected in this paper for avoiding overcorrecting the brightness values at larger angular locations where no significant echoes returned. It is found that multiecho regions occurred often in the radar volume even without beam-weighting correction, but we selected only the most intense echo region for study. In general, the zonal DOAs varied alternately between positive and negative values with time. On the other hand, the elevation DOAs of the echoes were negative and positive, respectively, at upper and lower parts of the FAI layer. Such a systematic variation in DOAs can be attributed to nonfilling effect in the radar volume; that is, it is not volume scattering condition, because the FAIs are highly localized and along the geomagnetic field lines. Fig. 4 shows a long FAI strip moving through the radar beam, with westward and southward drift components. The bulk drift motion is assumed to be propelled by the neutral wind, not the $\mathbf{E} \times \mathbf{B}$ drift of the meter-scale plasma irregularities in

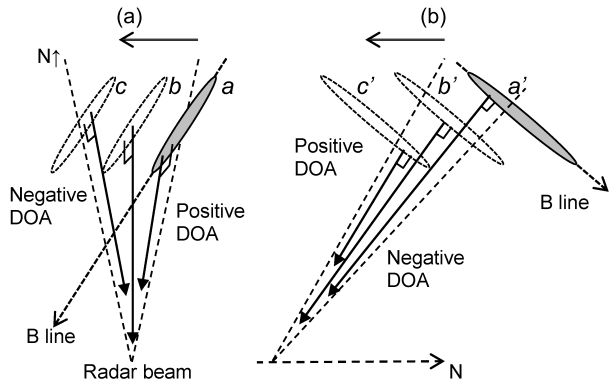

Fig. 4. Schematic of an FAI strip drifting through the radar beam in the zonal and meridional directions. Solid-lined arrows indicate the mean arrival directions of the echoes, which are perpendicular to the FAI strip and from different parts of the FAI strip. (a) Zonal drift. (b) Meridional drift.

the FAI layer [23]. The zonal DOA is defined as positive and negative for the echoes returned, respectively, from the eastern and western portions of the radar volume. As the FAI strip drifts through the radar volume, the zonal DOA changes alternately between positive and negative values with time, as observed in Fig. 3(c). The feature is the same when the FAI strip travels eastward. On the other hand, the meridional drift of FAI strip causes the elevation DOA negative and positive for the echoes returned, respectively, from the lower and upper parts of the radar volume. Such negative and positive DOAs occurred, respectively, at lower and higher ranges, as illustrated in Fig. 4(b). The feature retains the same for the FAI strip moving northward.

Variation in the elevation DOA with altitude/range has been notified in the study of polar mesosphere summer echoes (PMSEs) when using the oblique-beam CRI [31]. The PMSEs are horizontal echo layers confined within an altitude interval of several kilometers. For an oblique beam directed to arbitrary azimuthal angles, the upper and lower portions of the PMSE layer may fill the lower and upper parts of the radar volume, resulting in negative and positive DOAs, respectively.

In Fig. 4, the FAI strip at the time of *b* or *b*' is around the radar beam center, so the resultant DOA is expected to be around zero, and the echo power or SNR reaches its maximum. The FAI striations shown in Fig. 3(b) are numerous and close to each other, making the inspection of relationship between the SNR and the DOA difficult. To clarify such relationship, Fig. 5 demonstrates three more cases of FAIs. In the case shown in Fig. 5(a), the FAI striations were isolated. It can be observed that the zonal DOAs of each FAI strip varied from negative to positive as the time elapsed, implying an eastward drift motion. The meridional drift direction could be southward because of the negative range rate of FAI striations. The contour curves overlaying on the zonal DOA map show the SNR distribution, where the red curve indicates the approximate middle level of the SNR for highlighting the central echo region. It is evident that the maximum SNR was located between positive and negative DOAs, coinciding with that implied in Fig. 4.

Fig. 5(b) shows the case of FAIs with a positive range rate. In general, the zonal DOAs changed sign with time around

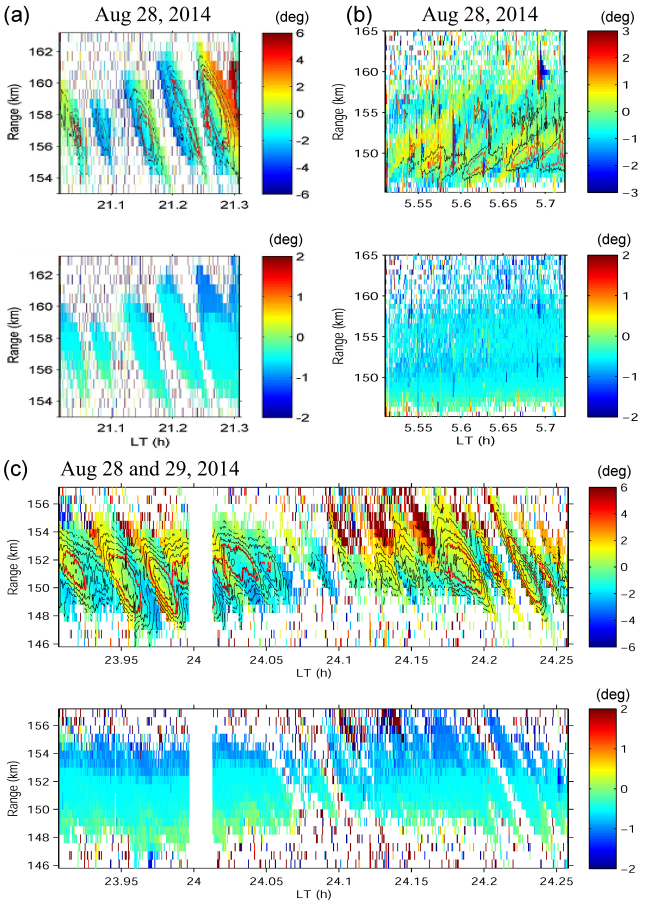

Fig. 5. (a)–(c) Three cases of FAIs observed on August 28 and 29, 2014. (Top) Off-beam zonal and (Bottom) elevation DOAs. The contour lines overlaying on the zonal DOA map show the SNR distribution, and the red curves indicate approximately the middle level of the SNR for highlighting the contour centers.

the range of 150 km where striation echoes occurred chiefly, as indicated by the SNR contour curves. Again, the maximum SNR was approximately located between positive and negative DOAs. In addition, the elevation DOAs have the same characteristic like that displayed in Fig. 3, regardless of negative or positive range rates.

Fig. 5(c) shows one more period of FAI echoes having temporal variation in the relationship between the SNR and the DOA. Before midnight, the zonal DOAs of the three FAI strips varied from positive to negative values, which was opposite to the case in Fig. 5(a) and implied a westward drift motion. However, at later time near 24.2 LT (00:12 LT), the zonal DOAs of the FAI strip changed from negative to positive values, which was similar to the case in Fig. 5(a). The signs of DOAs reversed again for the FAI strip just before 24.25 LT.

The zonal DOAs can indicate the zonal drift direction of FAIs. It is expected that the bulk drift velocity of FAIs, which is associated with the neutral wind, could be derived from the combination of zonal and elevation DOAs. Nevertheless, as shown in Fig. 4, the radar echoes may return from different parts of the FAI strip as the FAI strip drifts through the radar volume, making the estimate of bulk drift velocity-biased. According to Fig. 4, the DOA-estimated drift velocity

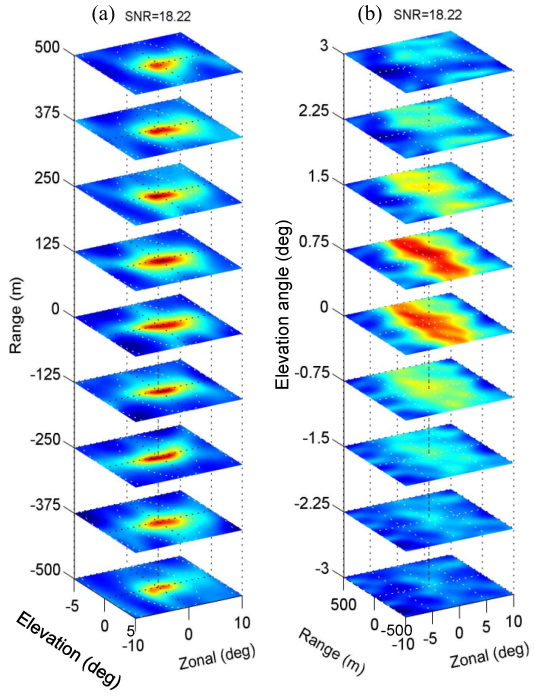

Fig. 6. 3-D radar imaging illustrated by several slices at (a) different ranges and (b) different off-beam elevation angles.

is smaller than the true value. Whether the 1-D and 2-D radar imaging can be applied to determination of bulk drift velocity of FAIs and then derive the neutral wind more precisely after some advanced treatments of DOAs, it can be a future issue. Multibeam, multireceiver, and multifrequency observations may be necessary for verifying the result. Before going deep into this issue, the 3-D radar imaging of FAIs in the radar volume was demonstrated first in this paper.

IV. 3-D Radar Imaging

We followed the Capon procedure and algorithm of 3-D radar imaging proposed in [1] and [4] and acquired the 3-D imaging of FAIs in the radar volume, as displayed in Fig. 6. Fig. 6(a) shows the slices at different range locations in the radar volume. The elevation dimension represents the off-beam angle in the meridional direction, where positive and negative angles mean, respectively, larger and smaller than the elevation angle of the radar beam. According to the 2011 IGRF model, the declination of geomagnetic field line (B line) was about 7.25° at an altitude of around 100 km above the MUR site (e.g., the occurrence height of E-region FAIs in the radar's viewing region); therefore, the elevation direction indicated in Fig. 6 was not exactly along the B line. Because the FAIs are highly aspect-sensitive along the B line, the FAI-echoes are confined within a small extent along the B line but may extend to several degrees in the zonal direction, depending on the radar beamwidth. These features are revealed in Fig. 6(a). Fig. 6(b) exhibits the slices at different off-beam angles in the meridional dimension. As seen, the echoes were confined to the vicinity of zero angle (the radar beam direction), and two or three strips in the range direction were resolved.

To demonstrate the 3-D structures in the radar volume in different ways, several brightness levels after normalization are shown in Fig. 7. Fig. 7(a) displays the case shown in Fig. 6. As seen, the brightness levels above 0.5 illustrate two FAI strips clearly. Fig. 7(a) (right) shows the result overlapping the levels between 0.5 and 1; the level step was 0.05. The overlapped map does not give a better presentation of the FAI structure for this case. By contrast, Fig. 7(b) shows another situation of FAIs, where the overlapped image reveals a bubblelike structure in the radar volume. Based on these illustrations, the 3-D radar imaging of FAIs is potentially workable for ionospheric studies, and more practical applications of 3-D radar imaging can be expected. In the following, we demonstrate an application of using the 3-D brightness distribution of radar imaging to investigate the declination of B line in the radar's viewing region.

V. Declination of Geomagnetic Line

Since the FAIs are localized along the B line and the radar beam is directed to the geographic north, the angular brightness distribution may reveal the declination of B line (D_B) even the echoes are highly aspect-sensitive along the B line. An example is shown in Fig. 8(a), where the angular brightness distributions at different range locations are illustrated. The angle step of imaging was 0.25°. First, the mean zonal locations of brightness values at different off-beam elevation angles were computed, as shown by the linked circle chain (like a thick curve) in each panel. We have discarded the mean brightness levels lower than 0.5 that occurred at larger off-beam elevation angles, and only the major brightness regions around the beam center were considered. A linear regression was then made for the linked circle chain to determine the slope of the brightness distribution, as shown by the sloping straight line. In this example, most of the regression lines indicated approximately the declination of B line in the radar volume except at the range locations above 150 m. In practical computing, the slope determined from the ratio of zonal versus elevation angles was estimated first to avoid quasi-vertical situation (a very large slope), providing the slope histogram shown in Fig. 8(b) for the echoes in Fig. 3. The reciprocal of the slope value in the histogram was the slope defined by the ratio of elevation versus zonal angles, giving the sloping straight line like that shown in Fig. 8(a). In Fig. 8(b), a Gaussian curve was used to fit the slope histogram, and the Gaussian peak location was the mean slope. Finally, the D_B angle was estimated according to $-\tan^{-1}$ (mean slope); it was $-7.31°$ in this example, very close to the value, $\sim -7.25°$, predicted by the 2011 IGRF model.

During computing, we noticed that the zonal extent of imaging and the SNR could alter the estimated D_B angle; therefore, calculations for different zonal extents were executed, and the results are shown in Fig. 8(c). Indeed, the estimated D_B angles depended on the zonal extent adopted in the computing and also depended on the SNR; they were larger than $-4°$ and close to zero as the SNR decreased to below $\sim$6 dB. In the situation of a lower SNR, the brightness distribution obtained from the Capon method diffuses more than that at a higher SNR, and it thus makes sense to have the D_B angles near

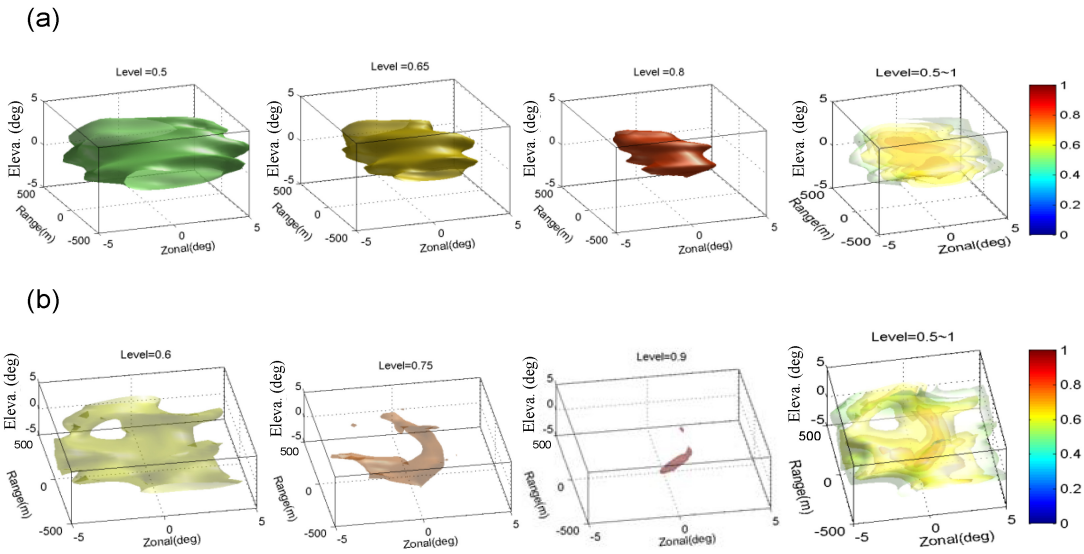

Fig. 7. Surface plots for different brightness levels after self-normalization, and the rightmost panels are the overlapped results between the levels of 0.5 and 1. (a) Case shown in Fig. 6. (b) Another situation in the same experiment.

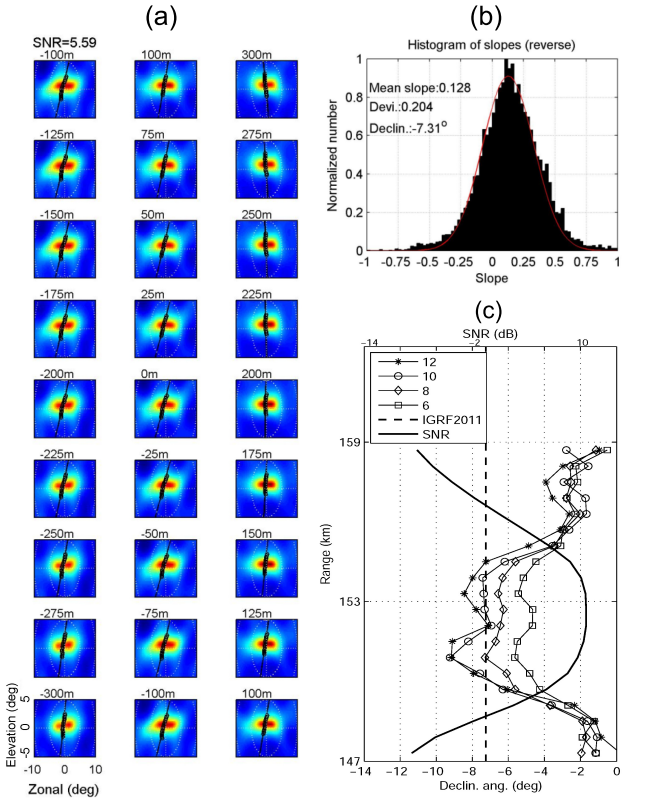

Fig. 8. (a) 3-D radar imaging illustrated by the slices at different ranges. The linked circles indicate the mean zonal locations at different off-beam elevation angles, and the sloping straight lines are the linear regression curves. (b) Slope histogram of the sloping straight lines for the data shown in Fig. 3, received at the range of 152.7 km. The slope was estimated initially from the ratio of zonal to elevation components, and the reciprocal of slope gives the sloping straight lines shown in (a). The peak location of the Gaussian-fitted curve is the mean slope, giving a mean declination angle, $-\tan^{-1}(\text{mean slope}) = -7.31°$. (c) Range profiles of mean declination angles obtained with different zonal extents (6°–12°). Vertical, bold dashed line: declination angle of the B line calculated from the 2011 IGRF model at the altitude of 100 km above the MUR location.

zero. On the other hand, around the range of 153 km where the SNR peaked, the estimated D_B angles were closer to the model-predicted value (indicated by the thick dashed-vertical line) as the zonal extent increased.

The range rates of the FAI striations examined in Fig. 8 were negative. For comparison, we investigated more FAI striations with positive range rates; the results are shown in Fig. 9. Binary complementary codes were employed in this observation, giving some artificial echoes (code-sidelobe echoes) at the locations above and below the source echoes, as seen in Fig. 9(a). Note that an ideal coding-decoding process with binary complementary codes has ideally zero range sidelobes, and therefore, these code-sidelobe echoes could be caused by the Doppler effects from fast movements and rapid variations of the targets [32].

The code-sidelobe echoes can be identified from the discontinuity of brightness distribution in the range direction, as shown in Fig. 9(b); they were discarded in the estimate of D_B. Fig. 9(c) presents the computed D_B angles. The mean SNRs were mostly larger than 9 dB through the range interval; however, the estimated D_B angles altered within a wider angular range and varied in accordance with the SNR, which were different from the previous case shown in Fig. 8. In spite of this difference, the estimated D_B angles still varied around the model-predicted value.

To validate further the D_B angles estimated from the brightness distribution, an additional experiment with the radar beam directed to 6.6° north by east was conducted on August 1 and 2, 2016. It is expected that the slope of brightness distribution governed by the slanted B line can be balanced off nearly due to the shift of beam direction, as indicated in Fig. 10(a). The dashed circle represents the cross section of radar beam, dash-lined arrow indicates the beam direction, solid-lined arrow shows the B line, and the dotted short line is the zonal direction in the imaging process that varies with the beam direction. Fig. 10(b) displays plentiful FAI striations having negative range rates. Notice that the radar operation was suspended for a while at around midnight, causing an apparent discontinuity of brightness values at that time, which does not influence the calculation. Fig. 10(c) shows the esti-

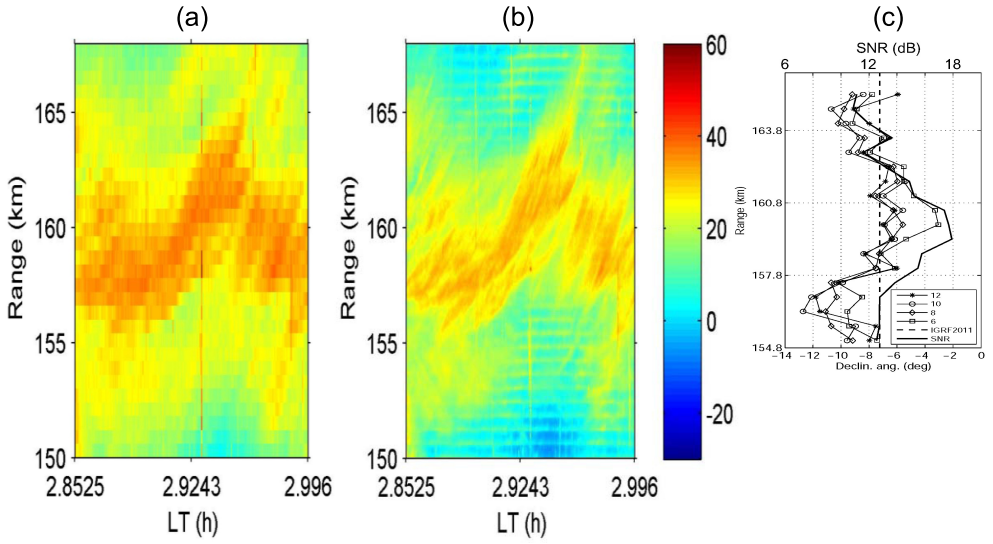

Fig. 9. FAIs having positive range rates, observed on August 17, 2014 with 16-bit complementary codes. (a) Range–time intensity. (b) RIM. (c) Range profiles of mean declination angles obtained with different zonal extents (6°–12°). The vertical, bold dashed line: declination angle of the B line calculated from the 2011 IGRF model at the altitude of 100 km above the MUR location.

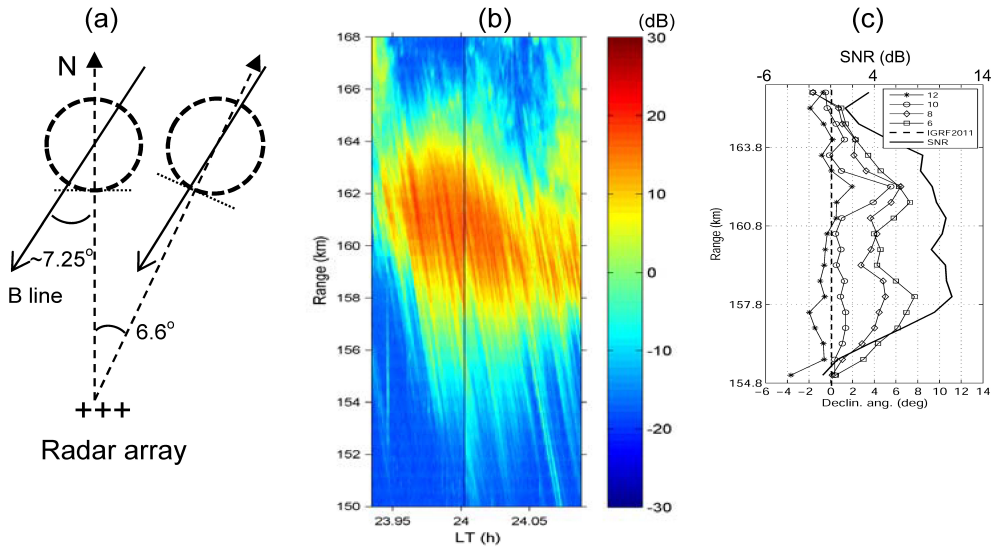

Fig. 10. Radar observation carried out on August 1 and 2, 2016 without phase codes. The radar beam was steered to 6.6° north by east and 51.5° zenith angle. (a) Schematic of radar beam direction. Dashed circle: cross section of radar beam. Dash-lined arrow: radar beam direction. Solid-lined arrow: geomagnetic field line. Short dotted line: zonal dimension in the imaging process that varies with the azimuthal direction of radar beam. (b) RIM. (c) Range profiles of mean declination angles obtained with different zonal extents (6°–12°). The vertical, bold dashed line: declination angle of the B line calculated from the 2011 IGRF model at the altitude of 100 km above the MUR location.

mated D_B angles that varied with the SNR, the range, and the zonal extent in the imaging process. As compared with Fig. 8(c), the estimated D_B angles shifted to positive values for the echoes having a larger SNR and still approached to zero for the echoes at a lower SNR. In general, we shall adopt the results of using 10° or 12° zonal extents, because more completed brightness distribution maps are obtained and thereby provide more reliable estimates. As expected, the D_B angles obtained from 10° or 12° zonal extents were closer to zero at a higher SNR, demonstrating the influence of the slanted B line has been balanced off.

VI. Conclusion

This is the first study of employing 3-D radar imaging technique to examine the ionospheric E-region FAIs in the radar volume. Five transmitter frequencies and 20 receiving channels were utilized in observation to achieve the 3-D radar imaging. 1-D RIM and 2-D angular imaging have also been performed.

The 1-D RIM not only produced sharper and smoother imaging of FAI striations but also revealed the locations of code-sidelobe echoes in the use of complementary codes, making the follow-up studies feasible. On the other hand, 2-D angular imaging provided angular brightness distribution and the DOA of the echoes. The off-beam zonal DOA changed sign alternately with time, which can be attributed to the zonal drift of the target. On the other hand, the off-beam elevation DOA was positive at lower range and eventually changed to negative values at higher range. This feature was assigned to the meridional drift of the target. Based on this, the DOA

seems applicable to estimate the bulk drift velocity of the FAIs propelled by the neutral wind. This issue, however, is still worth pursuing, because the echoes at different DOAs could return from different parts of the FAI striation, making the estimated drift velocity-biased. It is expected in the future that the 3-D structures of FAIs in the radar volume can improve the derivation of bulk drift velocity of FAIs, as long as the snapshot of FAIs is fast enough.

Examples of small-scale structures, such as FAI strips and bubblelike shape in the radar volume, have been shown. An application of 3-D radar imaging has also been demonstrated to be able to indicate the declination of a geomagnetic field line in the radar volume. The estimated declination of the geomagnetic field line was close to that predicted by the 2011 IGRF model.

ACKNOWLEDGMENT

All experiments were conducted with the support of the MUR International Collaborative Research Program, Research Institute for Sustainable Humanosphere, Kyoto University, Japan.

REFERENCES

[1] T.-Y. Yu and R. D. Palmer, "Atmospheric radar imaging using multiple-receiver and multiple-frequency techniques," *Radio Sci.*, vol. 36, no. 6, pp. 1493–1503, Nov./Dec. 2001, doi: 10.1029/2000RS002622.

[2] G. Hassenpflug, M. Yamamoto, H. Luce, and S. Fukao, "Description and demonstration of the new Middle and Upper atmosphere Radar imaging system: 1-D, 2-D, and 3-D imaging of troposphere and stratosphere," *Radio Sci.*, vol. 43, no. 2, Apr. 2008, Art. no. RS2013.

[3] T.-Y. Yu, J.-I. Furumoto, and M. Yamamoto, "Clutter suppression for high-resolution atmospheric observations using multiple receivers and multiple frequencies," *Radio Sci.*, vol. 45, no. 4, pp. 1–15, Aug. 2010, doi: 10.1029/2009RS004330.

[4] J.-S. Chen, C.-H. Chen, and J.-I. Furumoto, "Radar beam- and range-weighting effects on three-dimensional radar imaging for the atmosphere," *Radio Sci.*, vol. 46, no. 6, 2011, Art. no. RS6014, doi: 10.1029/2011RS004715.

[5] J.-S. Chen, J.-I. Furumoto, and M. Yamamoto, "Three-dimensional radar imaging of atmospheric layer and turbulence structures using multiple receivers and multiple frequencies," *Ann. Geophys.*, vol. 32, no. 8, pp. 899–909, 2014.

[6] R. Latteck *et al.*, "MAARSY: The new MST radar on Andøya—System description and first results," *Radio Sci.*, vol. 47, no. 1, 2012, Art. no. RS1006, doi: 10.1029/2011RS004775.

[7] J.-S. Chen, Y.-H. Chu, C.-L. Su, H. Hashiguchi, and Y. Li, "Range imaging of E-region field-aligned irregularities by using a multifrequency technique: Validation and initial results," *IEEE Trans. Geosci. Remote Sens.*, vol. 54, no. 7, pp. 3739–3749, Jul. 2016.

[8] M. Yamamoto, S. Fukao, R. F. Woodman, T. Ogawa, T. Tsuda, and S. Kato, "Mid-latitude E region field-aligned irregularities observed with the MU radar," *J. Geophys. Res., Space Phys.*, vol. 96, no. A9, pp. 15943–15949, Sep. 1991.

[9] C. J. Pan and R. T. Tsunoda, "Semidiurnal behavior of quasi-periodic echoes in the mid-latitude Es region observed with the Chung-Li VHF radar," *Geophys. Res. Lett.*, vol. 26, no. 16, pp. 2621–2624, 1999.

[10] C. J. Pan and M. F. Larsen, "Observations of QP radar echo structure consistent with neutral wind shear control of the initiation mechanism," *Geophys. Res. Lett.*, vol. 27, no. 6, pp. 867–870, 2000.

[11] F. Onoma *et al.*, "Relationship between propagation direction of gravity waves in OH and OI airglow images and VHF radar echo occurrence during the SEEK-2 campaign," *Ann. Geophys.*, vol. 23, no. 7, pp. 2385–2390, 2005.

[12] R. B. Cosgrove and R. T. Tsunoda, "A direction-dependent instability of sporadic-*E* layers in the nighttime midlatitude ionosphere," *Geophys. Res. Lett.*, vol. 29, no. 18, pp. 11-1–11-4, 2002, doi: 1029/2002GL014669.

[13] M. F. Larsen, "A shear instability seeding mechanism for quasiperiodic radar echoes," *J. Geophys. Res., Space Phys.*, vol. 105, no. A11, pp. 24931–24940, 2000.

[14] P. A. Bernhardt, "The modulation of sporadic-*E* layers by Kelvin–Helmholtz billows in the neutral atmosphere," *J. Atmos. Solar-Terrestrial Phys.*, vol. 64, nos. 12–14, pp. 1487–1504, 2002.

[15] M. F. Larsen, M. Yamamoto, S. Fukao, R. T. Tsunoda, and A. Saito, "Observations of neutral winds, wind shears, and wave structure during a sporadic-*E*/QP event," *Ann. Geophys.*, vol. 23, no. 7, pp. 2369–2375, 2005.

[16] R. D. Palmer, S. Gopalam, T.-Y. Yu, and S. Fukao, "Coherent radar imaging using Capon's method," *Radio Sci.*, vol. 33, no. 6, pp. 1585–1598, 1998.

[17] R. D. Palmer, T.-Y. Yu, and P. B. Chilson, "Range imaging using frequency diversity," *Radio Sci.*, vol. 34, no. 6, pp. 1485–1496, Nov./Dec. 1999.

[18] H. Luce, M. Yamamoto, S. Fukao, D. Helal, and M. Crochet, "A frequency domain radar interferometric imaging (FII) technique based on high-resolution methods," *J. Atmos. Solar-Terrestrial Phys.*, vol. 63, nos. 2–3, pp. 221–234, 2001.

[19] D. L. Hysell, M. Yamamoto, and S. Fukao, "Imaging radar observations and theory of type I and type II quasi-periodic echoes," *J. Geophys. Res., Space Phys.*, vol. 107, no. A11, pp. SIA7-1–SIA7-14, 2002, doi: 10.1029/2002JA009292.

[20] S. Saito, M. Yamamoto, H. Hashiguchi, and A. Maegawa, "Observation of three-dimensional structures of quasi-periodic echoes associated with mid-latitude sporadic-*E* layers by MU radar ultra-multi-channel system," *Geophys. Res. Lett.*, vol. 33, p. L14109, Jul. 2006, doi: 10.1029/2005GL025526.

[21] Y.-H. Chu and K.-F. Yang, "Reconstruction of spatial structure of thin layer in sporadic *E* region by using VHF coherent scatter radar," *Radio Sci.*, vol. 44, no. 5, pp. 1–17, Oct. 2009, doi: 10.1029/2008RS003911.

[22] C. Y. Wang, Y. H. Chu, C. L. Su, R.-M. Kuong, H.-C. Chen, and K. F. Yang, "Statistical investigations of layer-type and clump-type plasma structures of 3-m field-aligned irregularities in nighttime sporadic *E* region made with Chung-Li VHF radar," *J. Geophys. Res., Space Phys.*, vol. 116, no. A12, 2011, Art. no. A12311, doi: 10.1029/2011JA016696.

[23] Y. H. Chu, K. F. Yang, C. Y. Wang, and C. L. Su, "Meridional electric fields in layer-type and clump-type plasma structures in mid-latitude sporadic *E* region: Observations and plausible mechanisms," *J. Geophys. Res., Space Phys.*, vol. 118, pp. 1243–1254, Mar. 2013, doi: 10.1002/jgra.50191.

[24] D. L. Hysell, "Radar imaging of equatorial *F* region irregularities with maximum entropy interferometry," *Radio Sci.*, vol. 31, no. 6, pp. 1567–1578, 1996.

[25] J. L. Chau and R. F. Woodman, "Three-dimensional coherent radar imaging at Jicamarca: Comparison of different inversion techniques," *J. Atmos. Solar-Terrestrial Phys.*, vol. 63, nos. 2–3, pp. 253–261, 2001.

[26] J. L. Chau, D. L. Hysell, K. M. Kuyeng, and F. R. Galindo, "Phase calibration approaches for radar interferometry imaging configurations: Equatorial spread F results," *Ann. Geophys.*, vol. 26, no. 8, pp. 2333–2343, 2008, doi: 10.5194/angeo-26-2333-2008.

[27] R. D. Palmer, B. L. Cheong, M. W. Hoffman, S. J. Fraser, and F. J. López-Dekker, "Observations of the small-scale variability of precipitation using an imaging radar," *J. Atmos. Ocean. Technol.*, vol. 22, no. 8, pp. 1122–1137, 2005.

[28] J.-S. Chen and J.-I. Furumoto, "Measurement of atmospheric aspect sensitivity using coherent radar imaging after mitigation of radar beam weighting effect," *J. Atmos. Ocean. Technol.*, vol. 30, no. 2, pp. 245–259, 2013, doi: 10.1175/JTECH-D-12-00007.1.

[29] D. L. Hysell, J. Munk, and M. McCarrick, "Sporadic *E* ionization layers observed with radar imaging and ionospheric modification," *Geophys. Res. Lett.*, vol. 41, pp. 6987–6993, 2014, doi: 10.1002/2014GL061691.

[30] S. Fukao, T. Sato, T. Tsuda, M. Yamamoto, M. D. Yamanaka, and S. Kato, "MU radar: New capabilities and system calibrations," *Radio Sci.*, vol. 25, no. 4, pp. 477–485, 1990.

[31] S. Sommer, G. Stober, J. L. Chau, and R. Latteck, "Geometric considerations of polar mesospheric summer echoes in tilted beams using coherent radar imaging," *Adv. Radio Sci.*, vol. 12, pp. 197–203, Nov. 2014.

[32] K. Wakasugi and S. Fukao, "Sidelobe properties of a complementary code used in MST radar observations," *IEEE Trans. Geosci. Remote Sens.*, vol. GE-23, no. 1, pp. 57–59, Jan. 1985.

Jenn-Shyong Chen (M'11) was born in 1966. He received the B.S. and M.S. degrees in atmospheric physics and the Ph.D. degree in space science from National Central University (NCU), Taoyuan, Taiwan, in 1989, 1991, and 1998, respectively. He did his postdoctoral research at NCU and at Leibniz-Institut für Atmosphärenphysik, Kühlungsborn, Germany.

In 2002, he joined the Department of Computer and Communication Engineering (CCE), Chienkuo Technology University (CTU), Changhua, Taiwan. He has served as the Director of CCE, CTU, from 2010 to 2014, and as the acting Director of the Center for General Education, China Medical University, Taichung, Taiwan, from 2015 to 2016, where he is currently a Full Professor. His research interests include the techniques of multireceiver and multifrequency radar imaging and their applications to the atmosphere and the ocean.

Chien-Ya Wang was born in 1958. He received the Ph.D. degree in space science from National Central University, Taoyuan, Taiwan, in 1999.

Since 2000, he has been an Associate Professor with the Department of Optoelectric Physics, Chinese Culture University, Taipei, Taiwan. His research interests include radar remote sensing of the ionosphere.

Yen-Hsyang Chu was born in 1954. He received the Ph.D. degree in atmospheric physics from National Central University (NCU), Taoyuan, Taiwan, in 1988.

From 1988 to 1992, he was an Associate Professor with the Department of Atmospheric Physics, NCU, where he has been a Full Professor with the Graduate Institute of Space Science since 1993. He has served as the Director of the Graduate Institute of Space Science, NCU, from 1996 to 1999, as the Secretary General of NCU from 2006 to 2009, and as the Dean of the Research and Development Office, NCU, from 2009 to 2013. He is currently serving as the Dean of the College of Earth Science, NCU. His research interests include radar remote sensing of the atmosphere and ionosphere, retrieval of atmospheric refractivity profile using the GPS radio occultation technique, and radio wave propagation channel modeling.

Ching-Lun Su was born in 1969. He received the Ph.D. degree in space science from National Central University (NCU), Taoyuan, Taiwan, in 2004.

Since 2007, he has been a Project-Appointed Assistant Researcher with the Graduate Institute of Space Science, NCU. His research interests include radar remote sensing of the atmosphere and ionosphere.

Hiroyuki Hashiguchi received the bachelor's degree in electrical engineering from the Faculty of Engineering and Design, Kyoto Institute of Technology, Kyoto, Japan, in 1990. He completed the second half of his Ph.D. degree with the Department of Electrical Science and Engineering, Graduate School of Engineering, Kyoto University, Kyoto, in 1995.

In 1997, he became a Research Associate with the Radio Atmospheric Science Center, Kyoto University (reorganized in 2000 as the Radio Science Center for Space and Atmosphere). In 2001, he became an Associate Professor at the Radio Science Center for Space and Atmosphere, Kyoto University [reorganized in 2004 as the Research Institute for Sustainable Humanosphere (RISH)]. In 2018, he became a Professor at RISH. His research interests include the development of atmospheric radars and research on observations using their radars.

Dr. Hashiguchi is a member of the Meteorological Society of Japan, the Society of Geomagnetism and Earth, Planetary and Space Sciences, the American Meteorological Society, the American Geophysical Union, and the Institute of Electronics, Information and Communication Engineers, Japan. In 1992, he became a Research Fellow of the Japan Society for the Promotion of Science. He was a recipient of the 2006 Minister of Education Science and Technology Award and the 2008 Horiuchi Prize of the Meteorological Society of Japan.